Comparison of refraction inversion methods

Bernard Law and Daniel Trad

ABSTRACT

Near surface weathering statics correction are traditionally done using first arrival times. Generalized Linear Inversion (GLI) and refraction tomography are two commonly used methods. Both GLI and refraction tomography are ray based method and require velocity to varies slowly. Furthermore, GLI uses the delay time concept and requires layered medium with velocity varies slowly in the lateral direction only. Refraction tomography is based on ray traced refraction ray paths and can handle more complex near surface geology. Both algorithms can include model weight and data weight in the cost function to incorporate reflection residual statics measurements. The modified GLI and refraction tomography cost function can improve the stability of the solution; however, the methods use first arrival travel time picks and are limited by the high frequency asymptotic approximation. Full waveform inversion (FWI) updates the velocity model by minimizing the misfit between the recorded field data and the modeled wavefield. FWI can provide higher resolution model than ray theory based methods. We compare Both GLI and refraction tomography methods using synthetic model and field data. We also review the full wave form inversion method and use synthetic model to demonstrate its potential and limitations for refraction inversion.

INTRODUCTION

. First arrivals of refracted waves from seismic reflection surveys have been used to create near-surface velocity model for initial static correction for most land seismic data processing. There are many different methods to obtain near-surface velocity model from refraction arrival times. Refraction methods that uses layered model include delay time method (Gardner, 1939, Barry, 1967), plus-minus method (Hagedoorn, 1959), generalized reciprocal method (Palmer, 1981), generalized linear inversion (GLI) method (Hampson and Russell, 1984) and weathering layer tomography (Docherty, 1992). Some of these methods compute the velocity and thickness directly using refraction travel time equations and shot and receiver geometry. GLI and weathering layer tomography use inversion schemes to compute the thickness and velocity parameters by minimizing the misfits between the modeled and actual first arrival times. Turning-ray refraction tomography methods (White 1989; Zhu, Sixta and Angsman 1992; Belfer and Landa, 1996) discretize the near-surface velocity model into rectangular cells. Rays are traced through these cells between source and receivers by solving the ray equations (Cervany,1980; Langan, Lerche and Cutler, 1985; Vinje, 1993) or the Eikonal equation (Vidale, 1988; Qin, 1992; Sethian and Papovici, 1996). Turning-ray refraction tomography back propagates the misfits between the actual and ray traced first arrival times along the ray paths to update the velocity grid.

GLI method can provide stable solution; however, it is limited by the assumption of layered based refraction model with velocity increasing in depth. In area of complex

geological structures and surface terrain and when the velocity model is better represented by velocity gradients, the simplified assumption used in the delay time methods are often violated. Turning-ray tomography methods are not limited by this simple assumption. It can image near-surface velocity with higher resolution than delay-time method. However, it suffers instability when ray-density is low, especially at large shot point gaps and at edges of 2-D and 3-D survey. Starting model, grid size and smoothing parameters can also influence the final model of turning-ray tomography. Besides choosing the algorithm and parameters that best suite the near-surface geology, refraction data quality and acquisition geometry can also affect the refraction solution and correction. Therefor refraction statics corrections often contain errors caused by the quality of the refraction data, numerical errors of the refraction solution and the inability of the refraction algorithm to model the actual physical properties of the near-surface. This can result in unsatisfactory statics corrections and reflection images. These problems are often addressed by revising the parameters and constraints of the refraction algorithm and by surface consistent residual statics using deeper reflection data. Using a surface-consistent hypothesis Taner (1974) showed that surface consistent residual statics correction can yield optimally stacked CDP section with lateral signal continuity representative of real geology. Ronen and Claerbout (1985) demonstrated that surface-consistent residual statics can be estimated by stack-power maximization. Statics estimation is effectively a velocity analysis of the near-surface (Ronen and Claerbout, 1985); however, surface-consistent residual statics derived from more coherent and better sampled reflection data are not used in refraction inversion algorithms

High resolution near-surface velocity model from turning-ray refraction tomography is often integrated with reflection velocity model and used in depth imaging and depth model building processes. Uncertainties in near-surface velocity model derived from refraction data alone tend to accumulate and adversely affect the velocity building process of the deeper layers. Kosloff et al. (1997) and Pecholcs et al. (1997) used depth errors from subsurface image gathers to update velocity and thickness in the near-surface layers. Birdus et al. (2013) used velocity model from reflection tomography as the starting point for their iterative joint refraction/ reflection tomography workflow. The integrity of the reflections is the priority of this joint inversion. Law and Trad (2016) used the long wavelength components of the surface-consistent residual statics to constraint the GLI and refraction tomography solution by including the model weight and data weight terms in the cost functions of the GLI and refraction tomography methods. The modified GLI and refraction tomography cost function harmonizes the near surface velocity model with the reflection data. However, these methods are based on the ray theory, a high frequency asymptotic approximation of the wave theory. Ray theory based methods assumes infinitely high frequencies and require the velocity model to vary smoothly. Full waveform inversion (FWI) updates the velocity model by minimizing the misfit between the recorded field data and the modeled wavefield. FWI can provide higher resolution model than ray theory based methods.

THEORY

Refraction inversion

Refraction solution can be cast as the inversion of near-surface velocity model parameters ***m*** using first arrival time picks ***d*** and forward modeling operator ***L***:

$$d = L\,m\,, \tag{1}$$

where $L\,m$ is the modeled first arrival times. The model parameters ***m*** can be computed by minimizing the objective function ***J***:

$$J = \| d - Lm \|^2\,. \tag{2}$$

The least square solution of equation (2) is:

$$m = (\,L^T L)^{-1} L^T\,d \tag{3}$$

First arrival time can be modeled with layered model using delay time method or with grid model using turning-ray refraction tomography.

Delay time method

Delay time concept uses a simple refraction model depicted in Figure 1, where the total travel time from S to R can be expressed using delay times δSB and δCR, offset X and velocity V_1 :

$$T = \delta SB + \delta CR + \frac{X}{V_1} \tag{4}$$

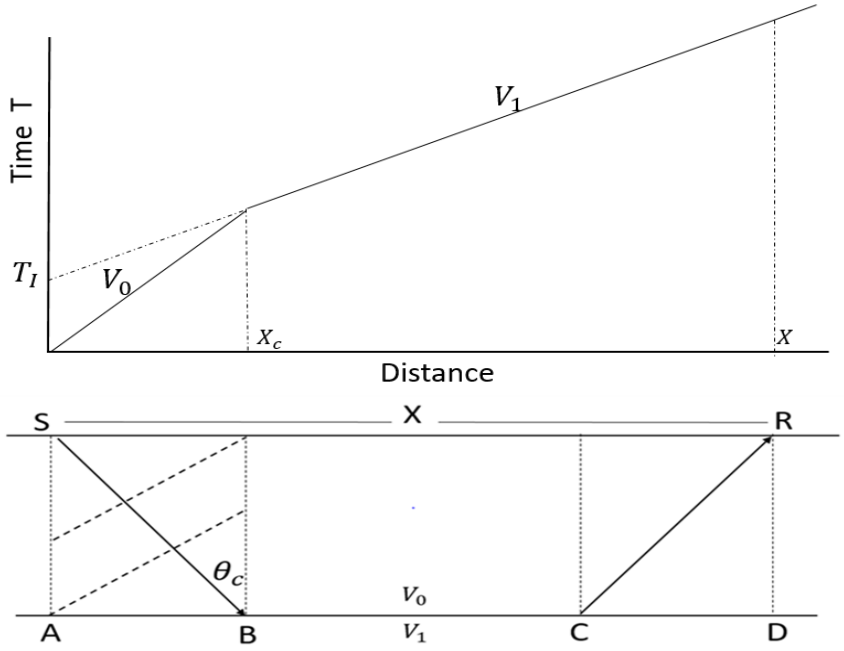

Figure 1. Refraction raypath and Time-Distance plot. Intercept time T_I equals the sum of delay times δSB and δCR.

Intercept time T_I in Figure 1 is the sum of the delay times δSB and δCR. Delay time is not an observable quantity, it represents the time to travel from the source or receiver to a refractor minus the travel time necessary to travel the normal projection of the raypath on

the refractor. Gardner (1939) showed that from ray path geometry and Snell's law delay time can be expressed as:

$$\delta SB = \frac{Z_1 \, x \, cos\theta_c}{V_0} \tag{5}$$

With equal thickness at S and R, equation (4) can be written for the n[th] layer as:

$$T_n = \int_{k=1}^{n} 2 \, \frac{Z_k \, cos\theta_{ck}}{V_{k-1}} + \frac{X}{V_n} \tag{6}$$

With the delay time concepts refractor velocity V_k and thickness of refractor Z_k can be computed using measurable traveltime and offset distance. $V_k \; and \; Z_k$ can also be computed by minimizing the cost function in equation (2). Hampson and Russell (1984) presented the GLI method that uses the delay time equation to compute the model perturbation via first order Taylor expansion and related the errors in T_n to the model perturbations in $V_k \; and \; Z_k$ using the following sets of linear equations:

$$\Delta T = B \Delta M \tag{7}$$

$$B = \partial T / \partial m \tag{8}$$

where ΔT is the changes in ray traced time between iterations and $\partial T / \partial m$ is the partial derivative of travel time with respect to the model parameters $V_k \; and \; Z_k$. Least square solution for ΔM is:

$$\Delta M = (B^T B)^{-1} \, \Delta T \tag{9}$$

Turning-ray refraction tomography

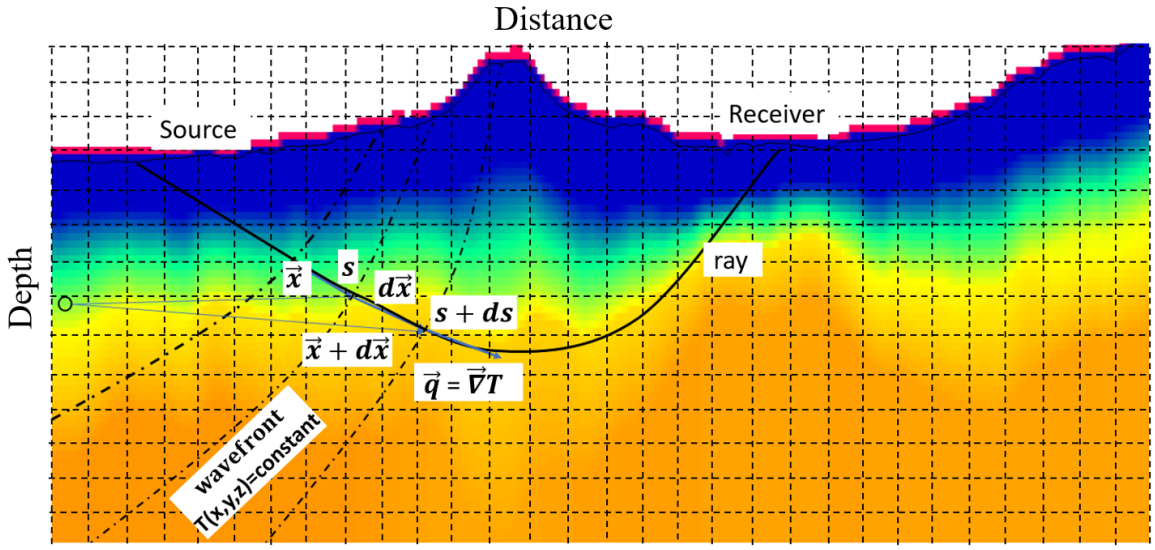

Figure 2. Relationship between ray path geometry and travel time.

Turning-ray refraction tomography methods discretize the near-surface velocity model into a grid of rectangular cells. Figure 2 shows a near-surface velocity grid and the relationship between ray path geometry and travel time. Rays are traced through the velocity cells between source and receivers using diving rays by solving the ray equations (10) and (11) or the Eikonal equation (12):

$$\frac{d\vec{x}}{ds} = c \, \vec{q} \quad , \tag{10}$$

$$\frac{d\vec{q}}{ds} = \vec{\nabla}\left[\frac{1}{c}\right], \tag{11}$$

$$\left(\frac{\partial T}{\partial x}\right)^2 + \left(\frac{\partial T}{\partial y}\right)^2 + \left(\frac{\partial T}{\partial z}\right)^2 = \frac{1}{c^2}, \tag{12}$$

where c is the velocity, $\vec{q}$ is the slowness vector, $\frac{d\vec{x}}{ds}$ is a unit vector tangential to the ray, and T is the travel time. If equation (10) and (12) are used to trace the ray, travel time can be computed by integrating the slowness model along the ray path. If the Eikonal equation is used to compute the travel time, ray path can be traced along the path of maximum travel time gradient (Vidale, 1988) or along the path of minimum time (Matsuoka,1992). Ray path distances within velocity cells form the forward modeling operator $\boldsymbol{L}$ in equation (1) and (2). Solving equation (3) will yield the slowness parameter, $\boldsymbol{m}$. Turning-ray tomography can also be solved as a discrete linear problem

$$\boldsymbol{G}\,\boldsymbol{m} = \boldsymbol{d}, \text{ and} \tag{13}$$

$$\boldsymbol{G} = \begin{bmatrix} L_{1,1} & L_{1,2} & .. & L_{1,m} \\ L_{2,1} & L_{2,2} & .. & L_{2,m} \\ .. & .. & .. & .. \\ L_{n,1} & L_{n,2} & .. & L_{n,m} \end{bmatrix}, \tag{14}$$

$$\boldsymbol{m} = [\Delta M_1 \quad \Delta M_2 \quad .. \quad \Delta M_n]^T, \tag{15}$$

$$\boldsymbol{d} = [\Delta T_1 \quad \Delta T_2 \quad .. \quad \Delta T_n]^T, \tag{16}$$

where $L_{i,j}$ is the ray segment length for ray path i and cell j, $\Delta M_j$is the model update for cell j, and ΔT_i is the difference between observed travel time and ray traced travel time. ΔM matrix can be solved directly with

$$m = (G^T G)^{-1} G^T d \quad . \tag{17}$$

Alternatively, we can use Simultaneous Iterative Reconstruction Technique (SIRT) (Lo and Inderwiesen, 1994; Dines and Lytle,1979) to solve for ΔM_j :

$$\Delta M_j = L_{ij} d_i / \sum_{j'=1}^{J} L^2{}_{ij'}, \tag{18}$$

where i is the observation number, j is the model cell to update, j' to J is the range of model cells that the ray path has traversed and L_{ij} is the ray segment length for observation number i and model cell j.

Incorporating reflection measurement in near-surface velocity model update

Errors in the refraction solution arise when the modeling operator **L** is unable to model the observed first arrival times because of poor refraction data quality, numerical errors of the refraction solution and the inability of the refraction algorithm to model the actual physical property of the near-surface. These problems are often revealed on CDP stack section as deterioration in reflection coherence and structural integrity. They are often compensated by applying surface consistent residual statics corrections derived from correlation of reflection data. These surface consistent statics corrections contain data error ϵ_d, numerical error ϵ_m and algorithm error ϵ_p in the refraction solution. In conventional refraction and reflection residual statics workflow, the surface consistent residual statics are applied to the reflection data to compensate for deficiencies in the near-surface velocity model; however, the near-surface velocity model is not updated. If the surface consistent residual statics are caused by the deficiencies in the near-surface velocity mode, we can back propagate these errors vertically to update the near-surface velocity model.

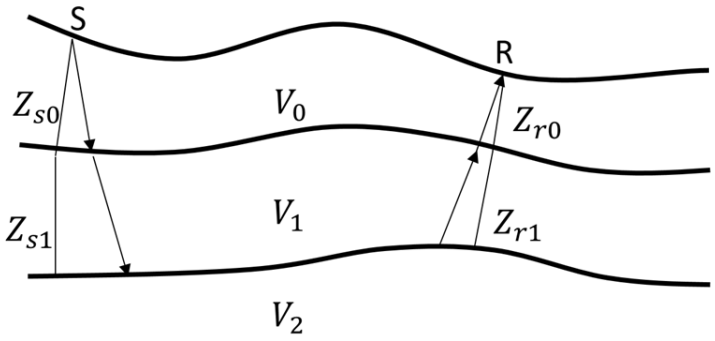

Figure 3. Refraction model and weathering statics correction

Consider a layered model shown in Figure 3, weathering statics correction is computed by

$$T = \sum_{i=0}^{n}(\frac{1}{Vr} - P_i)\, Zs_i + (\frac{1}{Vr} - P_i)\, Zr_i \quad , \tag{19}$$

where Zs_i and Zr_i are thickness of layer i at source and receiver location, V_i is the velocity for layer i and V_r is the replacement velocity for weathering statics correction. Defining

$$T_i = \frac{Z_i}{V_r} - Z_i P_i \,, \tag{20}$$

$$E = smoothed\ \ residual\ statics \quad , \tag{21}$$

$$E_i = E\,(\ \frac{Z_i}{Total\ thickness}\ )\,, \tag{22}$$

$$Z_i = Thickness\ for\ layer\ i \,, \tag{23}$$

$$P_i = \frac{1}{V_i}, \tag{24}$$

$$W_{mi}(slowness) = slowness\ model\ weight\ for\ layer\ i, \text{and} \tag{25}$$

$$W_{mi}(thickness) = thickness\ model\ weight\ for\ layer\ i \,, \tag{26}$$

where T_i is the weathering statics correction for layer i. Adding smoothed surface consistent statics correction E_i to the weathering statics correction T_i, and updating only P_i with $W_{mi}(slowness)$ yields:

$$T_i + E_i = \frac{Z_i}{V_r} - Z_i P_i W_{mi}(slowness)\,. \tag{27}$$

Equation (26) can be reduced to:

$$W_{mi}(slowness) = 1 - \frac{E_i}{Z_i P_i} \tag{28}$$

Similarly, updating only Z_i with $W_{mi}(thickness)$ yields:

$$W_{mi}(thickness) = 1 + \frac{E_i}{T_i} \tag{29}$$

To illustrate the concept of model weight, we create a finite difference synthetic dataset with a velocity model with 6 layers of velocities 1000, 2000, 2500, 3000, 3500 and 4000 m/sec. Both receiver spacing and depth step are 5 m. Two weathering pockets in the model are centered at station 251 and 601. Figure 4a shows the near-surface velocity model and synthetic shot record at station 500. Figure 4b compares the CDP

stack without weathering statics correction and the CDP stack with weathering statics correction using the actual model. Figure 4c shows the near-surface velocity model with error introduced, the CDP stack with weathering statics correction using the erroneous model and the surface consistent residual statics computed from reflection data. Figure 4d shows the updated velocity model $W_m m$, and the CDP stack with weathering statics correction from the updated velocity model. This synthetic data test demonstrates that incorrect near-surface velocity can reduce the coherency and structural integrity of reflection image. It also demonstrates that surface consistent reflection residual statics process can detect near-surface statics errors and the model weight W_m can be computed from these errors.

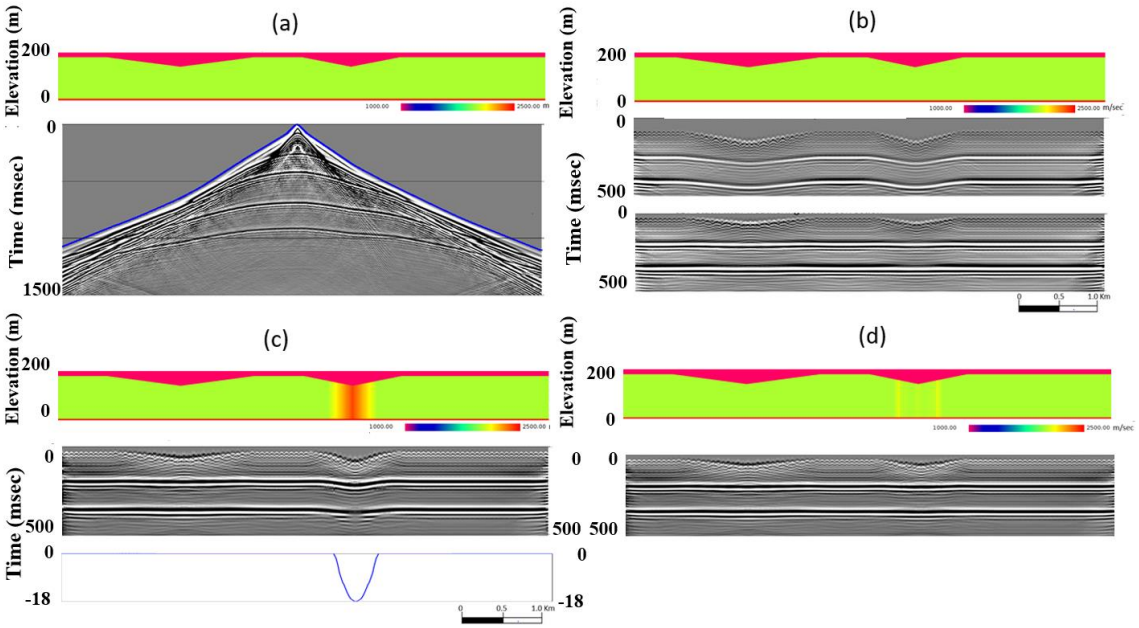

Figure 4. (a) Finite difference synthetic data with velocity variation in the near surface. (b) Comparison of CDP stack with and without weathering statics correction. (c) (top) Error introduced to near-surface velocity, (middle) CDP stack with weathering statics correction from model with error, (bottom) surface consistent residual statics from reflection data. (d) (middle) Modified near-surface velocity model using model weight.

Model and data space regularization

Data weighting function W_d, and imaging weighting function W_m in the cost function are a commonly used approach in geophysics (Claerbout 1992). Application of data weighting function and model weighting function is equivalent to data space and model space regularization. Regularization in data space helps to reduce the effects on the outlying picks on the solution. Regularization in model space stabilizes the solution and provides a mean of applying a priori information into the inversion (Zhou et al., 2013). Following an approach similar to Trad et al. (2015), we include the model weight W_m and data weight W_d in the cost function of the inversion problem,

$$J = \| W_d d - W_d L W_m m \|^2 . \quad (30)$$

When updating both slowness and thickness, W_{mi} (slowness) and W_{mi} (thickness) are:

$$W_{mi}(slowness) = 1 - 0.5\frac{E_i}{Z_i P_i} \quad , \tag{31}$$

$$W_{mi}(thickness) = 1 + 0.5\frac{E_i}{T_i} \quad , \quad \text{and} \tag{32}$$

$$W_d = \begin{matrix} 0 & E \geq \varepsilon \text{ and } \delta t > K \text{ x } std(\delta \text{t}) \\ 1 & otherwise \end{matrix} \tag{33}$$

where δt is the difference between observed and modeled first arrival time, $std(\delta t)$ is the standard deviation of δt, ε and K are thresholds used for W_d. We use equations (30) and (31) to compute W_{mi} (slowness) and W_{mi}(thickness) for the GLI algorithm. W_d corrects for data errors and is computed from the misfit between d and $L\,W_m m$.

For turning-ray tomography, W_m can be computed with

$$W_m \text{ (slowness)} = 1 - 0.5E/T \ , \tag{34}$$

$$W_m \text{ (thickness)} = 1 + 0.5E/T \ , \text{ and} \tag{35}$$

$$T = \sum_{iz=1}^{idatum} \left(\frac{1}{Vr} - P_{iz} \right) dz \ , \tag{36}$$

where $idatum$ is number of depth steps to the intermediate datum and P_{iz} is slowness at depth step iz. W_m and W_d can be incorporated into the turning-ray refraction tomography as:

$$W_d\, G\, W_m\, m = W_d\, d \tag{37}$$

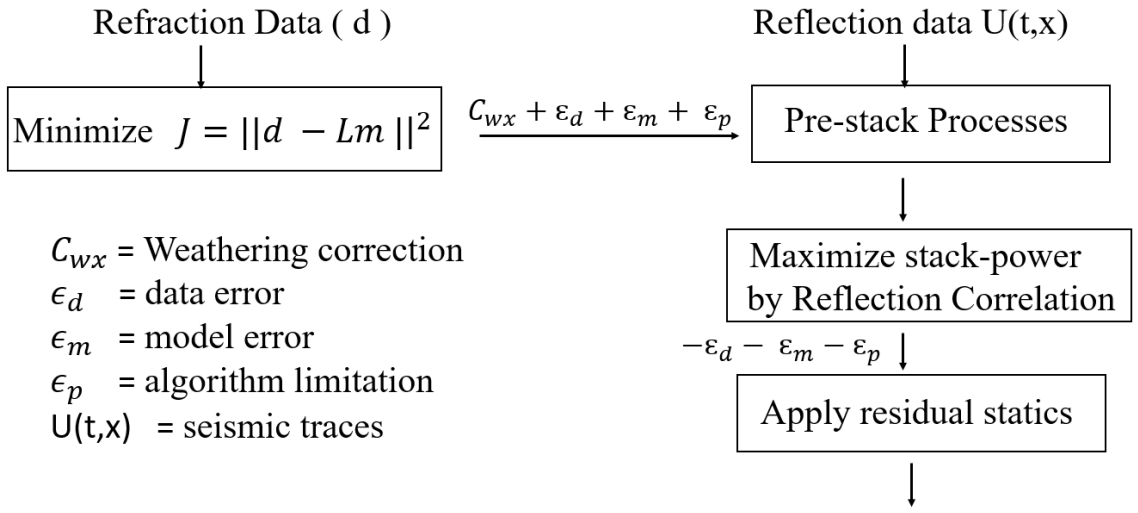

Figure 5. Conventional refraction and reflection statics workflow.

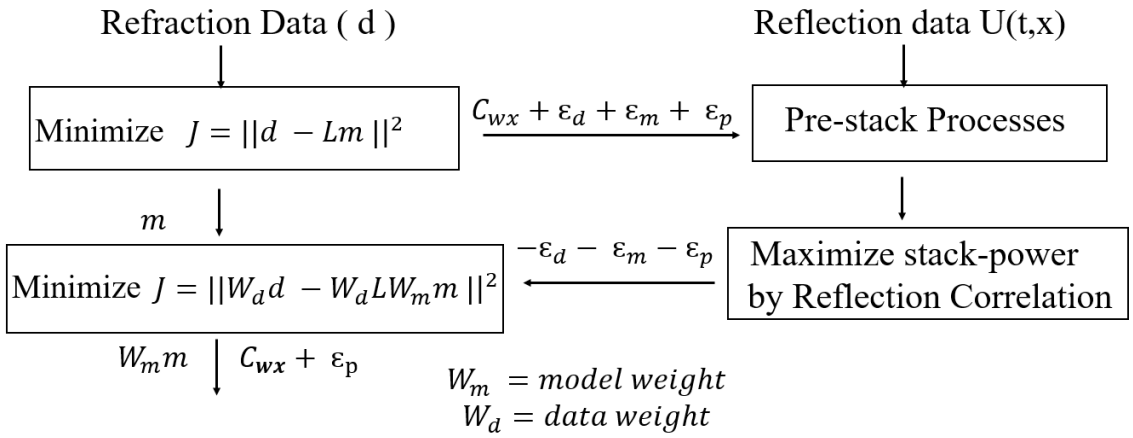

Figure 6. Nonlinear optimization of near-surface velocity model

Inversion procedure

1. Minimize $J = \| d - L\, m \|^2$ and apply weathering statics correction to seismic data
2. Compute surface consistent reflection residual statics.
3. Compute smoothed surface consistent residual statics E , $W_m$and W_d
4. If required, repick first arrival times using modeled first arrival times $W_m L\, m$ as constraints
5. Minimize $J = \| W_d d - W_d L\, W_m m \|^2$
6. Iterate 2 to 5 until convergence criteria are met

Weathering statics correction computed from the initial update model $W_m m$ is equivalent to applying smoothed surface consistent residual statics E to the seismic data. Subsequent iterations of minimizing $\| W_d d - W_d L\, W_m m \|^2$ will produce a near-surface velocity model that is in harmony with reflection data and can produce better imaging results.

Full waveform inversion

Full waveform inversion uses both refraction and reflection energy to reconstruct the physical properties of the earth. It refines the parameter model by minimizing the misfit between the predicted wavefield and the recorded wavefield:

$$\mathrm{E(m)} = \frac{1}{2}\sum_{r=1}^{ng}\ \sum_{s=1}^{ns}\int_0^{t_{\max}}\ |\, p_{cal}(\mathrm{x_r}, \mathrm{t};\ \mathrm{x_s}) - p_{obs}(\mathrm{x_r}, \mathrm{t}; \mathrm{x_s})|^2 \qquad (39)$$

where p_{cal} is the modeled seismic data, p_{obs} is recorded seismic data and E(m) is the misfit function to be minimized. Taylor expansion of (39) is:

$$\mathrm{E(m}\ + \Delta m) \approx E(m\,) + \frac{\partial E(m\,)}{\partial m}\Delta m \qquad (40)$$

and the partial derivative of (40) with respect to m is:

$$\frac{\partial \mathrm{E(m}\ + \Delta m)}{\partial m} \approx \frac{\partial E(m\,)}{\partial m} + \frac{\partial^2 E(m\,)}{\partial m^2}\Delta m \qquad (41)$$

hence, when $\frac{\partial \mathrm{E}(\mathrm{m}_0+\Delta m)}{\partial m} = 0$, model perturbation Δm is:

$$\Delta m = -\left[\frac{\partial^2 E(m)}{\partial m^2}\right]^{-1} \frac{\partial E(m)}{\partial m} \quad (42)$$

$$\Delta m = -H^{-1}\nabla E_m \quad (43)$$

where H represents the Hessian and ∇ represents the gradient. The gradient of the misfit function is given by (Bunks et al.,1995; Yang et al., 2015):

$$\nabla \mathrm{E_m} = \frac{2}{v^3(x)} \sum_{r=1}^{ng} \sum_{s=1}^{ns} \int_0^{t_{\max}} \frac{\partial^2 p_{cal}(\mathrm{x},\mathrm{t};\mathrm{x_s})}{\partial t^2}\, p_{res}(\mathrm{x_r},\mathrm{t};\ \mathrm{x_s})\mathrm{dt} \quad (44)$$

where $p_{res}(\mathrm{x_r},\mathrm{t};\ \mathrm{x_s})$ is the back propagated residual wavefield. For gradient or steepest decent methods, H^{-1} is replaced by the step length α (Virieux and Operto, 2009):

$$\Delta m = -\alpha \nabla E_m \quad (45)$$

Therefore, to update the velocity model, FWI iteratively computes the gradient $\nabla \mathrm{E}_m$ using the forward modelled wavefield and back propagated residual wavefield and computes the step length α using steepest decent methods. The gradient $\nabla \mathrm{E}_m$ is often referred to as the sensitivity kernel or wavepath (Woodward 1992). Figure 7 shows the gradients from a near offset and a far offset trace. The gradient from the near offset trace shows the model updating is along refraction wavepath as well as reflection wavepath. For the far offset trace of this experiment, the model update is primarily along the refraction wavepath.

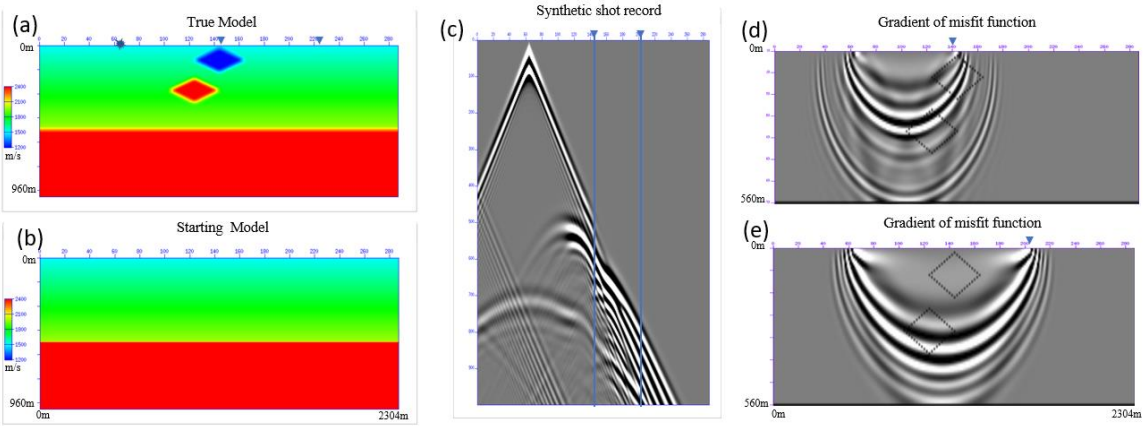

Figure 7: Gradients from FWI experiment (a) True model with 2 diamond shape velocity perturbations as well a flat velocity perturbation at 560 m depth. Source is located at surface station 64. Trace 144 and 204 are used to create two separative velocity updating gradient. (b) Starting model with the actual background velocity. (c) Synthetic shot record using the true model and 15 Hz Ricker wavelet. (d) and (e) gradient of misfit function from trace 144 and 204.

The relationship between FWI resolution and acquisition geometry can also be illustrated by the experimental setup of diffraction tomography(Figure 8) and the relationship between wavenumber **k**, frequency f, velocity c_0, aperture angle θ and **n**, the unit vector of the slowness vector **q**:

$$\mathbf{k} = \frac{2\mathrm{f}}{\mathrm{c}_0}\cos\left(\frac{\theta}{2}\right)\boldsymbol{n} \tag{46}$$

To reconstruct the large wavelength or small wavenumber medium low frequency data and wide aperture angle are required. For narrow-aperture acquisition geometry, both small and large wavenumber medium can be reconstructed by direct waves, refraction and reflection in the shallow area; while only small wavelength or large wavenumber medium is reconstructed by reflection in the deeper area.

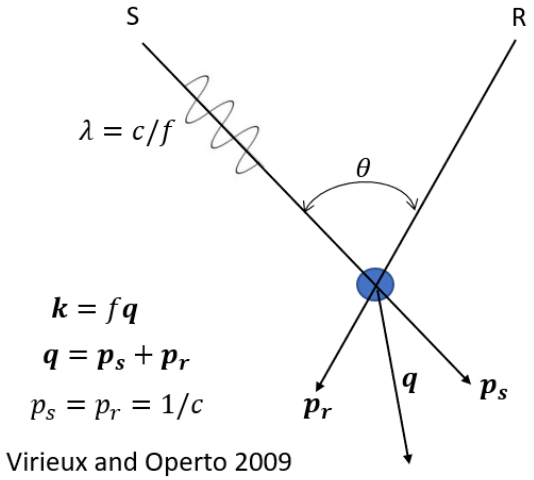

Fig 8: Relationship between FWI resolution and parameters in diffraction tomography: λ,wavelength; c, velocity; f, frequency; k, wavenumber; θ, aperture angle; p_s, p_r, q, the slowness vectors. S and R are source and receivers.

FILED DATA EXAMPLE

Conventional refraction statics and reflection residual statics processing flow and the proposed nonlinear optimization of near-surface velocity model processing flow are outlined in Figure 5 and 6. CDP stack sections are created using near-surface velocity models computed from the two processing flows. The data used in this example are the vertical component of the dynamite shot records from a 4.5 Km 2D 3C survey acquired at Hussar, Alberta in September 2011. The seismic survey was acquired for a broadband experiment (Margrave et al., 2010). It was also used for a S-wave statics investigation (Cova et al., 2017). Figure 9a and 9b show the location and the layout of the seismic line.

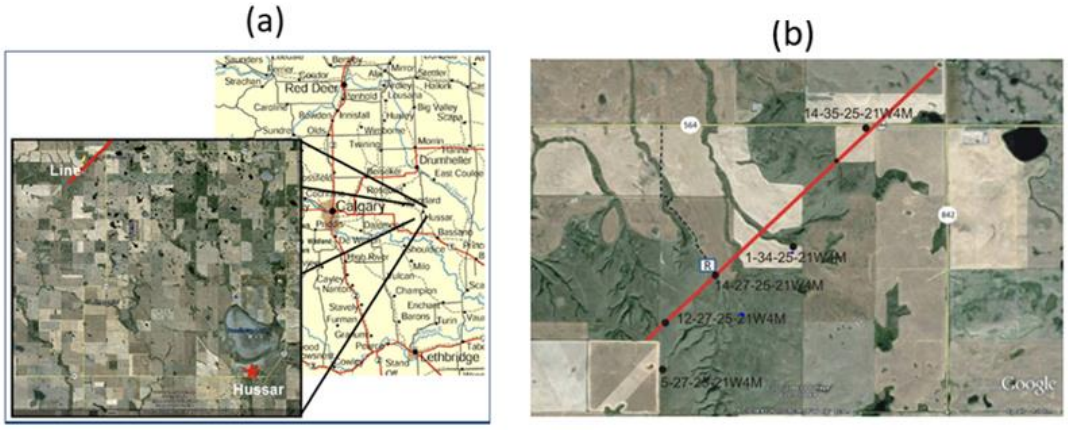

Figure 9. Hussar 2D broadband experiment (a) location map, (b) seismic line layout.

The seismic line runs NE-SW with a topographic relief of about 80 m. Receiver interval is 10 m and shot point interval is 20 m. The 448 channel split-spread geometry gives a nominal maximum offset of 2240 m for standard spread and maximum offset of 4480 for offend shots. First arrivals were picked for all traces and offsets; however, only first arrivals with offset less than 3000 m were used in the refraction solution. We created the common-receiver stack (Figure 10) and the CDP stack (Figure 11) with datum statics correction only. Effects of near-surface time delays are obvious on the common receiver stack. The incoherency of seismic events on the CDP stack is likely the result of the same near-surface time delays.

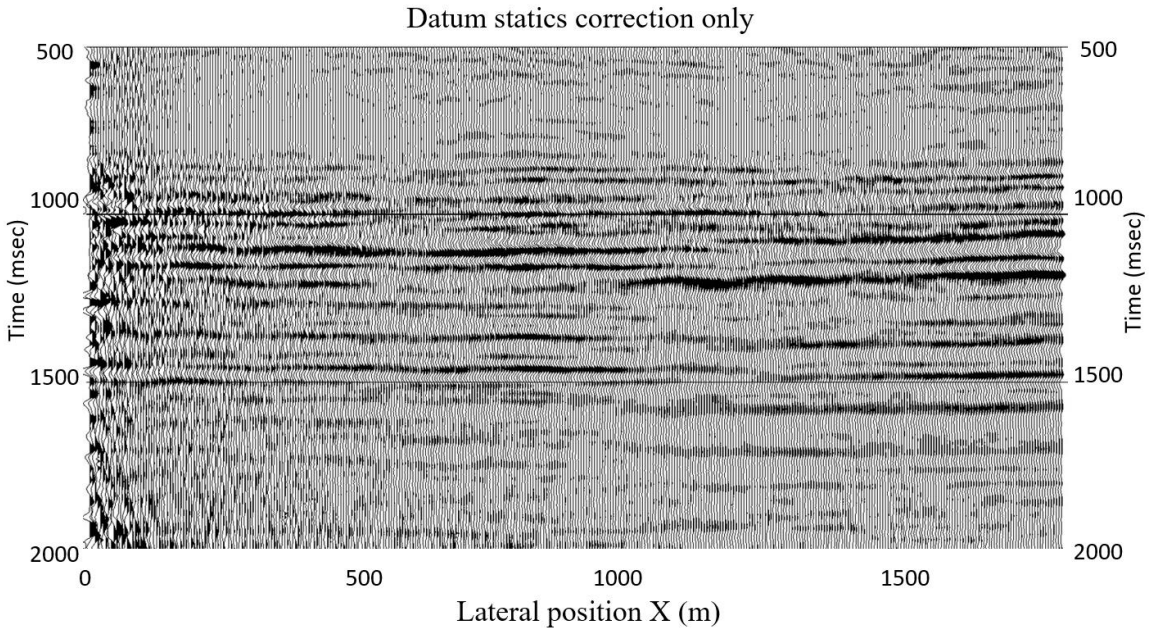

Figure 10. Common receiver

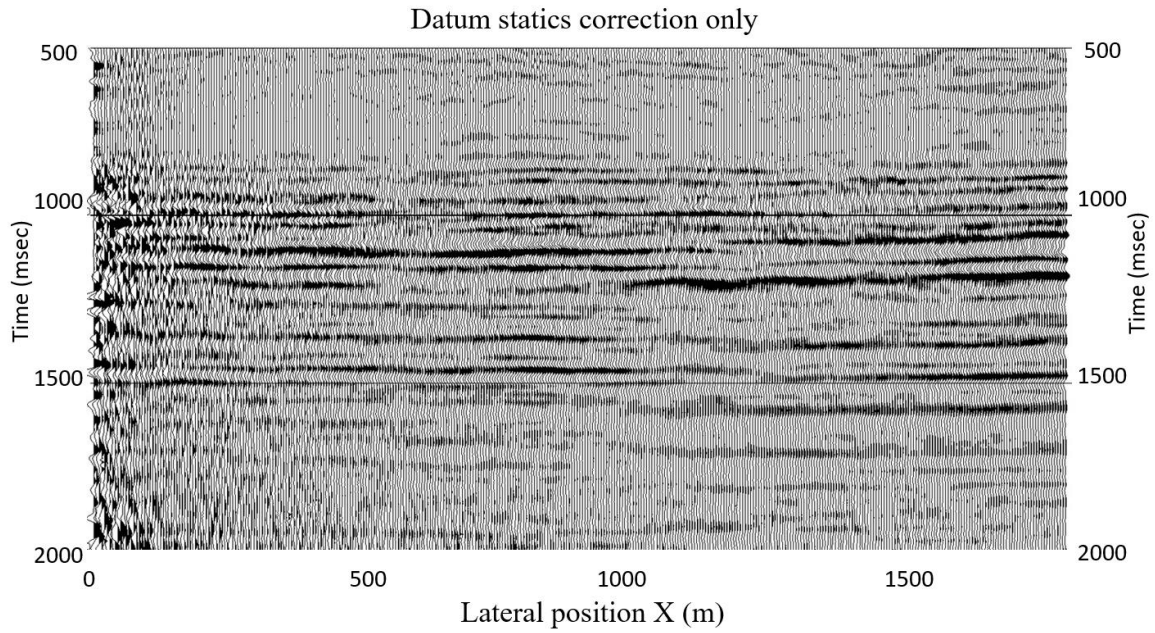

Figure 11. CDP stack with datum statics correction only

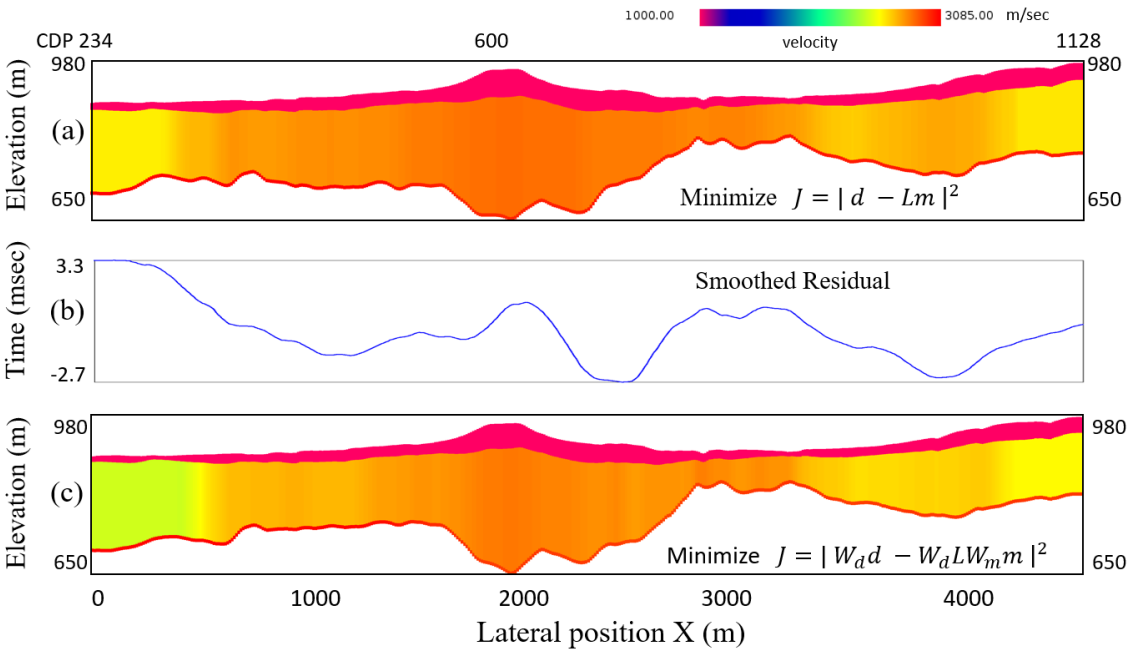

Figure 12. (a) GLI near-surface velocity model computed from minimizing the original cost function. (b) Smoothed surface-consistent residual statics. (c) Near-surface velocity model computed from the new cost function with model and data weights derived from smoothed surface consistent reflection residual statics.

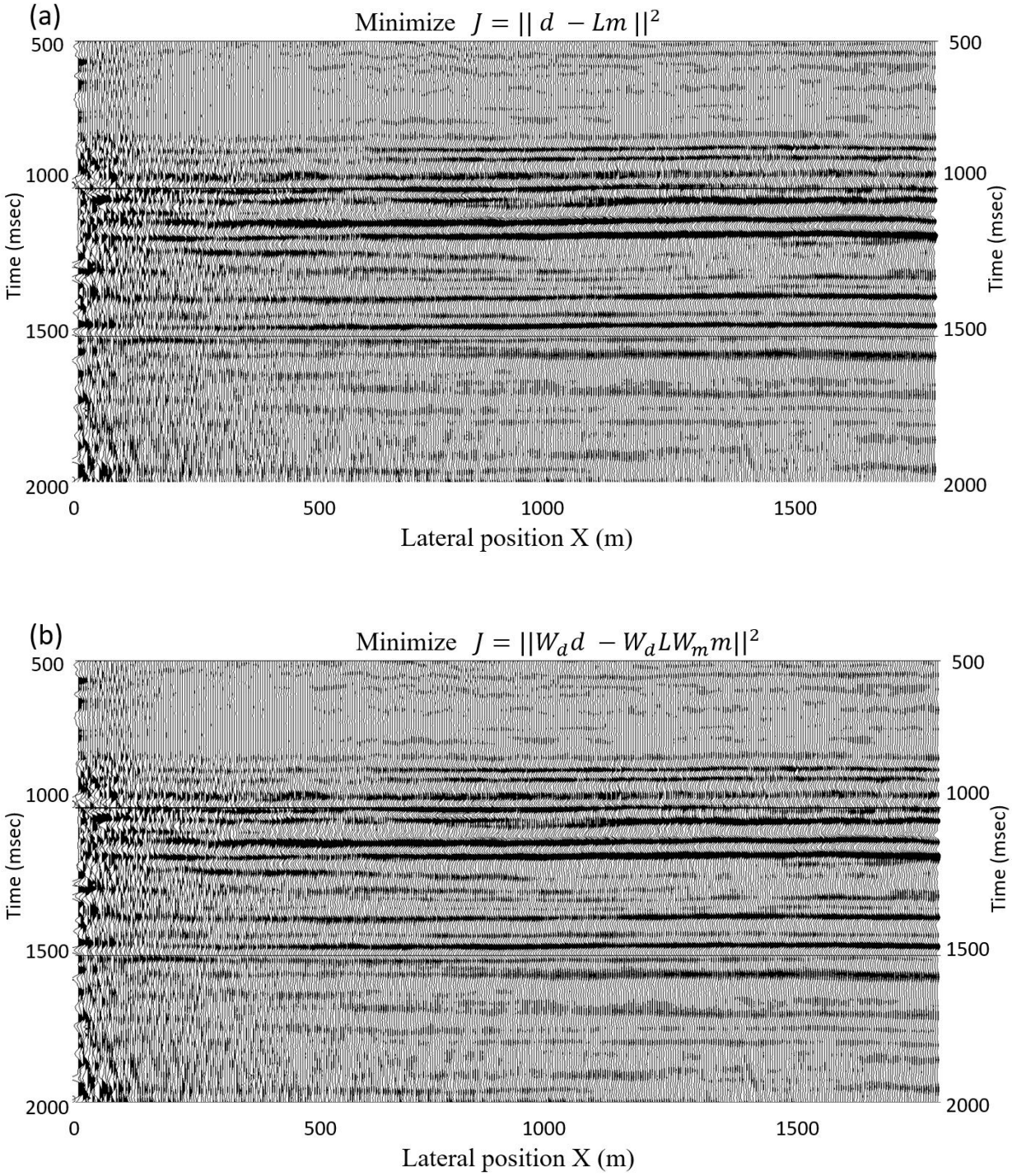

Figure 13. CDP stack section with weathering statics correction using GLI velocity model computed from minimizing (a) the original cost function, (b) the new cost function with model weight and data weight derived from surface constant reflection residual statics.

To test the proposed nonlinear optimization workflow for near-surface velocity model, we follow the steps outlined in figure 6. We create the first near-surface velocity

model by minimizing $\| d - Lm \|^2$ for both GLI and turning-ray refraction tomography. We then use the weathering statics corrected gathers from both methods to compute surface consistent reflection residual statics. We smooth the surface consistent residual statics and use them to compute the model weight W_m. Threshold parameter of 2 times the standard deviation of traveltime residual is used for W_d. Near-surface velocity model is then updated iteratively by minimizing $\| W_d d - W_d L W_m m \|^2$. Figure 10 and 11 compares the GLI solutions from the two processing flows. Figure 12 and 13 compares the turning-ray refraction solutions.

The smoothed surface-consistent reflection residual statics (Figure 10b) from gathers corrected with GLI solution from the original cost function are in the range of -2.7 to 3.3 msec. They are small; however, a long wavelength trend dipping from SW to NE can be observed at the NE end of the seismic line. The difference between the GLI solutions (Figure 10a and 10c) is small and occurs mostly at the two ends of the profile. CDP stacks with weathering statics correction from the two GLI methods (Figure 11a and 11b) show significant improvement in coherence and structural integrity when compared to the CDP stack with datum statics correction only. There is no significant difference in coherence between the two CDP stacks with GLI correction. However, the long wavelength trend difference is also found in the CDP stacks; with the structures in the CDP stack from the new workflow appear to be more reliable.

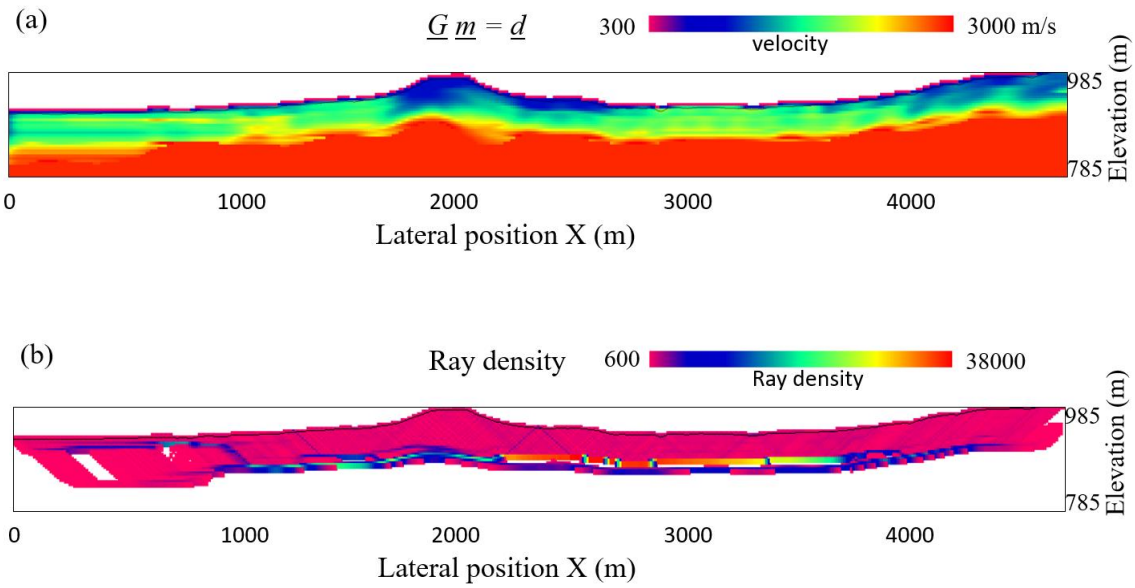

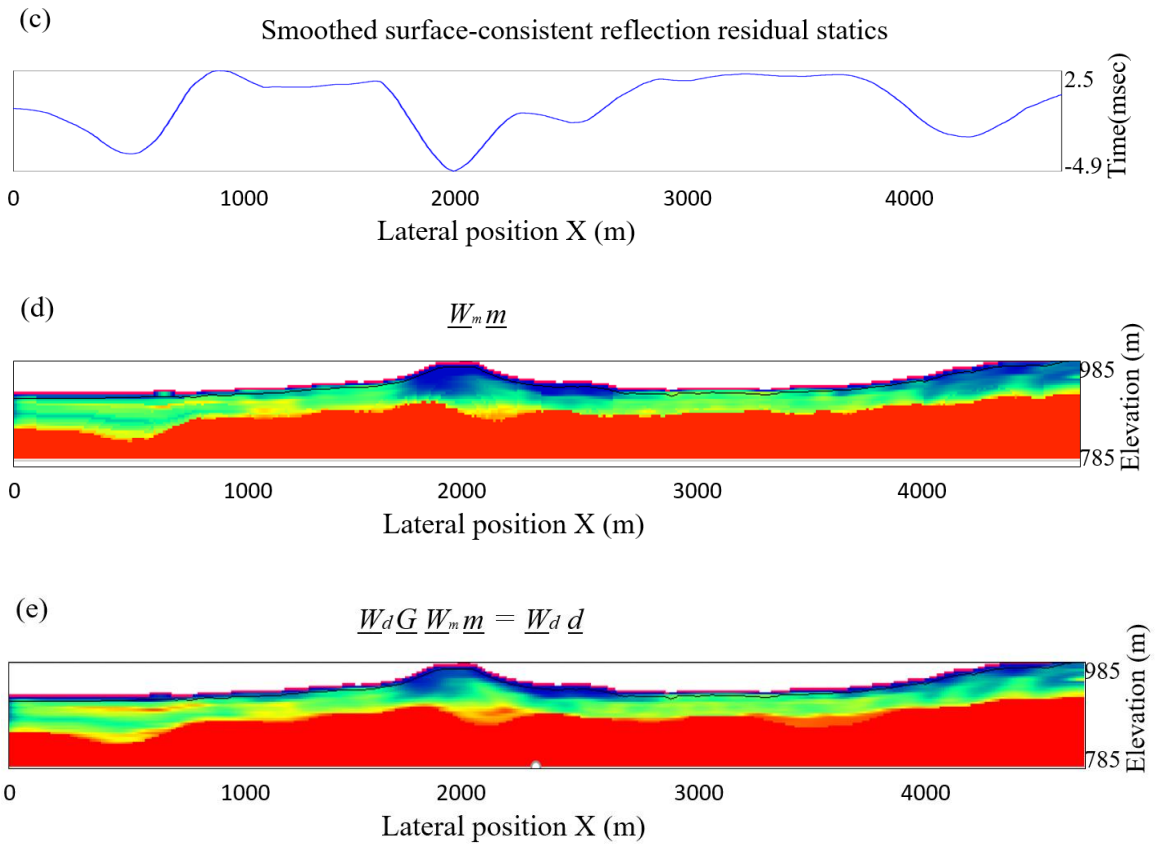

Figure 14. Turning-ray refraction tomography: (a) final model by solving $G\,m = d$, (b) ray density plot shows low coverage at edges of the model, (c) smoothed surface-consistent reflection residual statics, (d) updated model $W_m\,m$, (e) final model by solving $W_d G W_m m = W_d\,d$.

The results of turning-ray refraction tomography test are summarized in Figure 14a to 14e. As shown in the ray density plot (Figure 14b), not all cells are covered by ray paths. The minimum non-zero ray density of 600 and maximum ray density of 38000 seem high. However, for 448 channel recording with 269 shots and 488 receivers, ray coverage immediate below a shot point can be 448 channels plus 448 receivers. If a velocity cell is covered by every ray paths, the maximum possible ray density is 269 shots x 448 channels. Therefore, the ray density range of 600 to 38000 is reasonable. Velocity values at cells with no ray coverage cannot be updated and velocity values at cells with insufficient ray coverage can be unreliable. The smoothed surface-consistent reflection residual statics (Figure 14c) from gathers corrected with tomography solution from the original cost function are in the range of -4.9 to 2.5 msec. We do not see the similar long wavelength trend at the NE end of the seismic line as observed in the GLI solutions; however, a long wavelength trend can be observed at location between 1.0 Km to 2.0 Km from the start of the seismic line. We choose to update the model thickness instead of velocity, because applying the model weight for velocity puts the velocity into an unreasonable range. The updated velocity model $W_m m$ and the final velocity model after 7 iterations of the new kernel are shown in Figure 12d and 12e.

The CDP stack with the new turning-ray refraction tomography solution (Figure 15b) shows significant improvement in coherence at location between 1.0 Km to 2.0 Km from the start of the seismic line. Amplitudes of seismic events at around 1.0 second is slight weaker on the CDP stack with the new solution. This suggests NMO velocity may have to be revised after the new statics solution. On the CDP stack with the original turning-ray refraction tomography solution (Figure 15a), there is a long wavelength trend dipping from NE to SW. This trend is reduced on the CDP stack with the new solution.

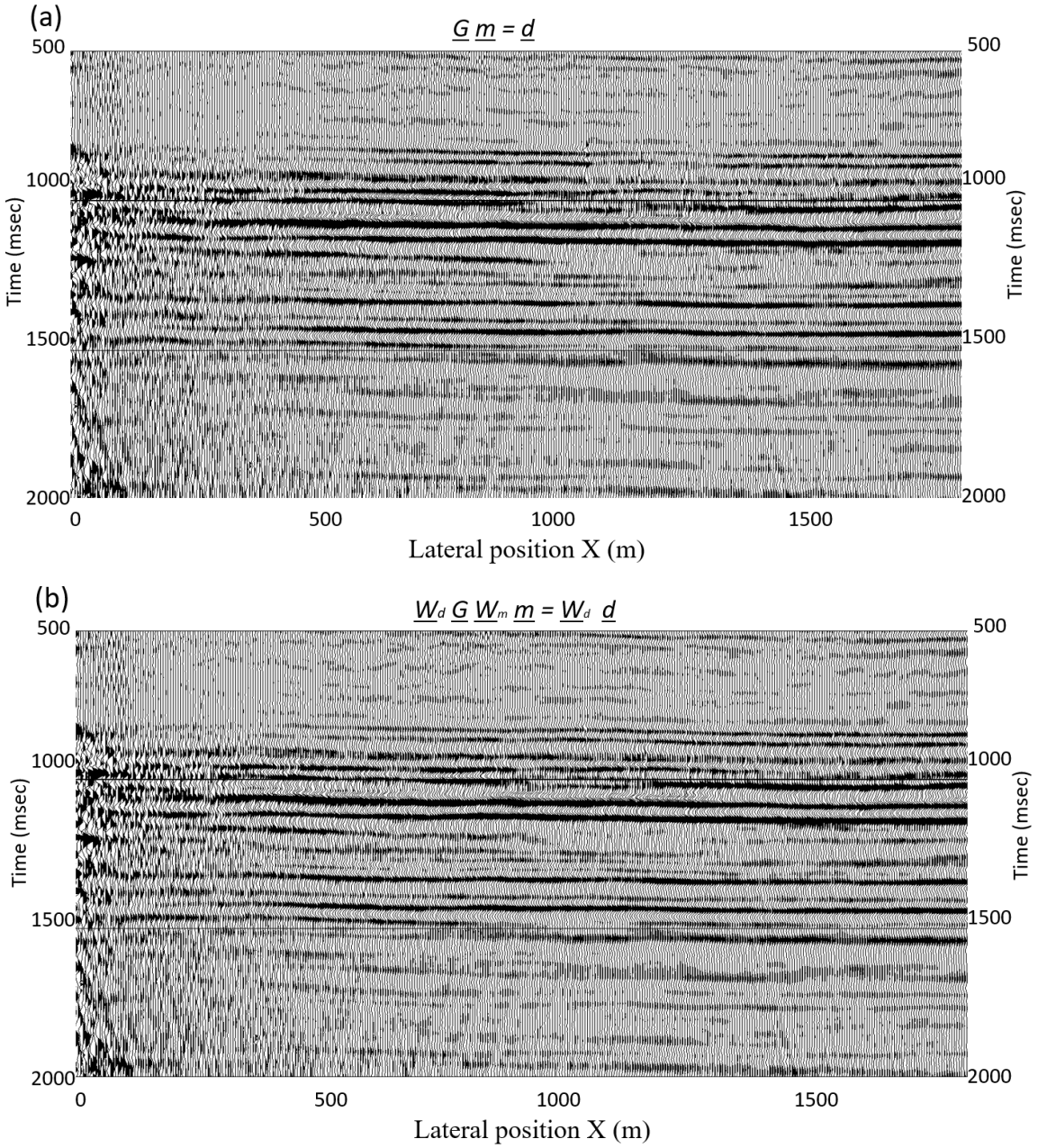

Figure 15. CDP stack section with weathering statics correction using turning-ray refraction tomography velocity model computed from solving (a) the original cost

function, (b) $W_d G\, W_m m = W_d d$ with model weight and data weight derived from surface constant reflection residual statics.

FWI NUMERICAL EXAMPLE

To evaluate the FWI resolution for near surface model reconstruction, we use a velocity model consists of a constant gradient background velocity with spatial variation in the shallow and several high wavenumber velocity perturbations represented by rectangular blocks (Figure 16a). Synthetic shot record (Figure 16b) of this model shows the upper most high wavenumber perturbation is captured by both refraction and reflection energy while the deeper high wavenumber perturbations are captured by reflection energy only. The velocity profiles of the true and starting models (Figure 16d) shows the low wavenumber and large wavenumber differences between the true model (Figure 16a) and the starting model (Figure 16c). Figure 17c shows the final FWI model after 118 iterations. Figure 17d shows the velocity profiles of the true model and the FWI result. In this test FWI resolves the large and short wavelength of the model at the shallow area. The errors increase near the edges of the model due to reduction in coverage. This noise free synthetic test demonstrated that FWI can resolve short wavelength variation in the model at the shallow and deep areas of the model as well as large wavelength variation with large aperture wavepaths in shallow area of the model. However, with more complex model and data noise resolving low wavenumber or large wavelengths of the medium can be more challenging.

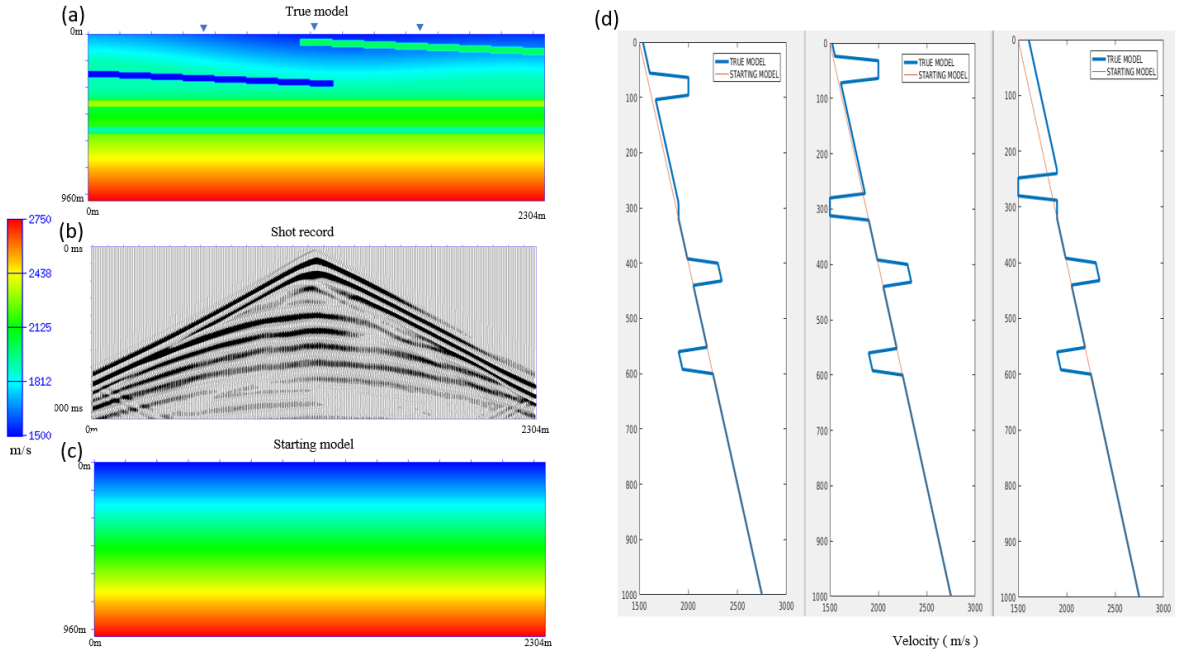

Figure 16: (a) True model for FWI test. (b) Synthetic shot record. (c) Starting model. (d) Velocity profiles of true and starting model

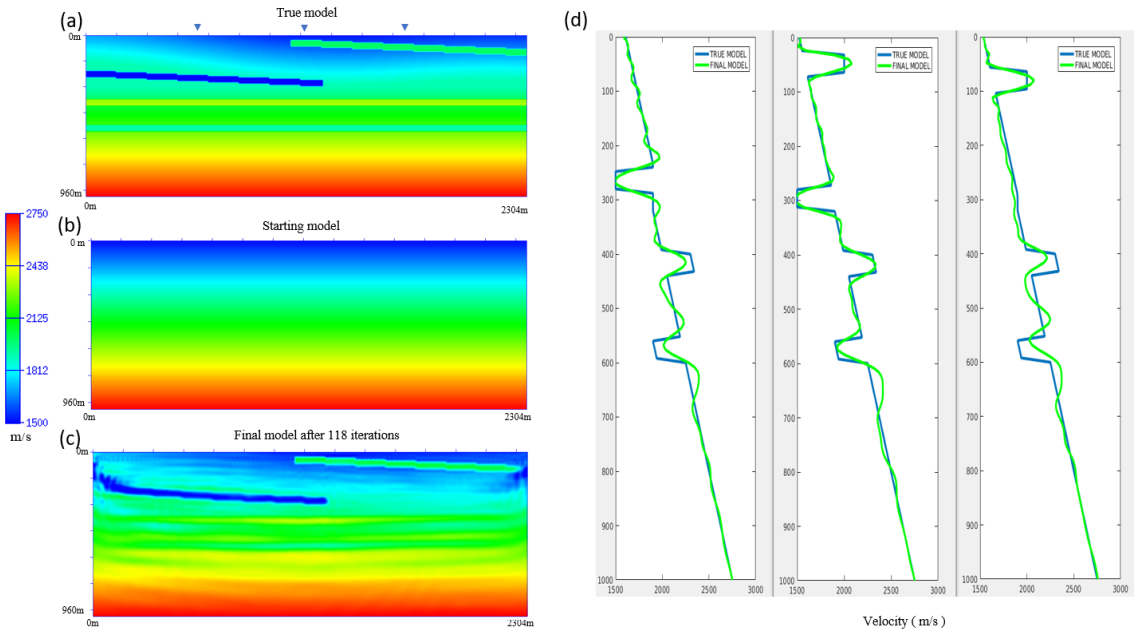

Figure 17:(a) True model for FWI test. (b) Starting model. (c) FWI final model after 118 iteratons. (d) Velocity profiles of true model and final FWI model.

DISCUSSION

Reliability of the refraction inversion can be improved by incorporating additional information from the seismic data and other seismic measurements. Surface-consistent reflection residual statics derived from correlation of reflection data optimize the stacking response of the reflection data. Using these statics corrections as errors failed to be detected in the near-surface refraction analysis and back projecting these errors to the near-surface velocity model can produce weathering statics correction that gives the same stacking response as applying the surface-consistent reflection residual statics. Using only the smoothed surface-consistent reflection residual statics helps to alter only the medium to long wavelength variations in the new-surface velocity model. We only apply a constant correction to all depth steps below the same surface location; however, this correction serves only as a priori information to guide the refraction inversion toward time delays that agree with the reflection data. With proper selection of the data weight threshold, optimal solution can be achieved by rejecting outlying picks. We suggest that the data weight threshold and choices of applying model weight to velocity, thickness or both should be tested. Decision should be made based on the coherence and structural integrity of the reflection image as well as the plausibility of the near-surface velocity model.

FWI uses the differences between the full wavefield of the modeled and measured seismic data to invert for the physical properties of the earth. For near surface imaging, FWI can resolve the small and large wavelengths of the medium and should produce a higher resolution result than refraction travel time inversion methods. However, when

the low frequency and wide aperture data is lacking, the reconstruction of large wavelengths of the medium can be challenging and using the near surface model from refraction travel time inversion as the starting model may be required. Moreover, when the differences between the modeled and measured wavefield do not agree with the physics of the forward modeling algorithm, the result of FWI can be unreliable. Therefore, careful preparation of the input data with consideration for noise, amplitude and removal of wave forms that are not part of the forward modeling process will be required.

CONCLUSION

We reviewed the GLI and refraction tomography methods and showed that conventional refraction inversion using first arrival times alone suffers from data errors, numerical errors and algorithm errors inherent in refraction data and refraction methods. Surface-consistent residual statics using correlation of reflection data can compensate some of these deficiencies in the near-surface velocity model by maximizing the stack response of the reflection data; however, the near-surface velocity model is left compromised by these errors. These deficiencies in the new-surface velocity model tend to accumulate in the deeper reflectors during subsequent reflection velocity model building processes. In contrast to the conventional refraction inversion that uses first arrival times alone, the new nonlinear optimization scheme uses also the surface-consistent reflection residual statics that maximize the stacking response as a priori information in the refraction inversion. This is implemented by modifying the cost function of refraction inversion to include model weight and data weight. We applied this scheme to GLI and turning-ray refraction tomography methods. Test results from the Hussar 2D dataset confirm that the proposed nonlinear optimization refraction solution workflow is robust and converges to a near-surface velocity model that is harmonized with the surface consistency of the reflection data. We have also used numerical experiment to demonstrate the resolving power of FWI. However, careful preparation of the input data to ensure the input to FWI matches the assumption and physics of forward modeling is critical for successful FWI.

ACKNOWLEDGMENTS

The authors would like to thank the sponsors and staffs of the Consortium of Research in Elastic Waves Exploration Seismology (CREWES). This work was funded by CREWES industrial sponsors and the Nature Science and Engineering Research Council of Canada through grant no. CRDPJ 461179-13.

REFERENCES

Barry, K. M., 1967, Delay time and its application to refraction profile interpretation in

Belfer, I., and E. Landa, 1996, Shallow velocity-depth model imaging by refraction tomography: Geophysical Prospecting, **44**, 859-870.

Birdus, S., D. Criddle, A. Artyomov, and Q. Tang, 2013, Successful application of joint reflection/refraction tomographic inversion in shallow water marine environment: 23rd Geophysical Conference ,ASEG Extended Abstracts:1-4.

Bunks, C.,F.M. Saleck, S.,Zaleski, and G. Chavent, 1995, Multiscale seismic waveform inversion: Geophysics,60,1457-1473.

Cerveny,V., and F., Hron.,1980. The ray series method and dynamic ray tracing system for three-dimensional inhomogeneous media: Bulletin seismological Society of America, **70**,47-77

Claerbout, J., 1992, Earth sounding analysis: Processing versus inversion: Blackwell Scientific Publ., Inc.

Cova, R., D. Henley, X. Wei, and K.A. Innanen, Receiver-side near-surface corrections in the $\tau - p$ domain: A raypath-consistent solution for converted wave processing: Geophysics, **82**, U13-U23.

Dines, K., and R. J. Lytle, 1979, Computerized geophysical tomography: Proceedings of the Institute of Electrical and Electronics Engineers,**67**,1065-1073.

Gardner, L., 1939, An area1 plan of mapping subsurface structure by refraction shooting: Geophysics, **4**, 247-259.

Gardner, L., 1967. Refraction seismograph profile interpretation, in Musgrave, A. W., Ed., Seismic refraction prospecting: Society of Exploration Geophysicist, 338-347.

Hagedoorn, J. , 1959, The plus-minus method of interpreting seismic refraction sections: Geophysical Prospecting, **7**, 158-182.

Hampson, D., and B. Russell, 1984, First Break Interpretation using generalized linear inversion: Journal of the Canadian Society of Exploration Geophysicists, **20**, 40-54.

Kosloff, D., U. Zackhem, and Z. Koren, 1997, Subsurface velocity determination by grid tomography of depth migrated gather: 67th Annual International Meeting, SEG, Expanded Abstracts, 1815-1818.

Kosloff, D., P. Pecholc, U. Zackhem and Z. Koren, 1997, Estimation of long wavelength near surface velocity and low-relief structure anomalies Part 2:A new near surface reconstruction method: 67th Annual International Meeting, SEG, Technical Expanded Abstracts 1997: 1063-1065

Langan, R., I. Lerche, R. Cutler, T. Bishop and N. Spera, 1984, Seismic tomography: The accurate and efficient tracing of rays through heterogeneous media: 54th Annual International Meeting, SEG, Expanded Abstracts, 713-715.

Lo, T.W., and P. Inderwiesen, 1994; Fundamentals of Seismic Tomography, SEG Geophysical monograph series, No. 6.

Margrave, G., M. Bertram, K. Hal, K. Innanen, D. Lawton, L. Mewhort, and T. Philips, 2012, A low-frequency seismic field experiment: 82nd Annual International Meeting, SEG, Expanded Abstracts, 454-457.

Matsuoka, T., and T. Ezaka, 1992. Ray tracing using reciprocity: Geophysics, **57**, 326-33.

Musgrave, A. W., Ed., Seismic refraction prospecting: Society of Exploration Geophysicist, 348-361.

Palmer, D., 1981, An introduction to the generalized reciprocal method of seismic refraction interpretation: Geophysics 46:1508-1518.

Pecholc, P., S. Nguyen, D. Kosloff and A. Litvin, 1997, Estimation of long wavelength near surface velocity and low-relief structure anomalies Part 2:A case history in central Saudi Arabia:67th Annual International Meeting, SEG, Expanded Abstracts: 1059-1062.

Qin, F., Luo, Y., Olsen, K., Cai, W., & Schuster, G. (1992). Finite-difference solution of the eikonal equation along expanding wavefronts: Geophysics, **57**, 478-487.

Ronen,J. and J. Claerbout, 1985, Surface-consistent residual statics estimation by stack-power maximization: Geophysics, **50**, 2759-2767

Sethian,J. and A. Popovici, 1999. 3-D traveltime computation using the fast marching method: Geophysics, **65**,516-523

Taner, M., and F. Koehler, and K. Alhilali, 1974, Estimation and correction of near-surface time anomalies: Geophysics,**39**, 441-463

Vidale, J.E.,1988. Finite difference calculation of travel times: Bulletin Seismological Society of America**,78**,2062-76.

Vidale, J. E., 1990, Finite-difference calculation of traveltimes in three dimensions: Geophysics, **55**, 521–526.

Vinje, V., E. Iverson, and H. Gjøystdal, 1993, Traveltime and amplitude estimation using wavefront construction: Geophysics, **58**, 1157–1166.

Virieux, J., and S. Operto, 2009, An overview of full-waveform inversion in exploration geophysics: Geophysics, **74**, No. 6,WCC127-WCC152.

White, D. J., 1989, Two-dimensional seismic refraction tomography: Geophysical Journal International, **97**,223-245.

Woodward, J., 1992, Wave-equation tomography: Geophysics, **57**, No.1,15-26

Yang, P., J. Gao, and B. Gao,2015, A graphics processing unit implementation of time-Domain full-waveform inversion: Geophysics, 80, No. 3, F31-F39.

Zhou, H., S. Gray, J. Young, D. Pham, D., and Y. Zhang,2002, Tomographic Residual Curvature Analysis: The Process and its Components: 72th Annual International Meeting, SEG, Expanded Abstracts, 666-669.

Zhu, X., D. Xita, B. Angstman, 1992, Tomostatics: Turning-ray Tomography + Statics Correction: The Leading Edge, **11**, no. 12, 15-23